Peer-reviewed version available at *Actuators* **2018**, *7*, 88; doi:10.3390/act7040088

Article

Car Soundproof Improvement Through an SMA Adaptive System

Salvatore Ameduri [1], Angela Brindisi [1], Monica Ciminello [1], Antonio Concilio [1,*], Vincenzo Quaranta [1] and Marco Brandizzi [2]

[1] Centro Italiano Ricerche Aerospaziali; cirascpa@legalmail.it
[2] Centro Ricerche Fiat; crf-comunicazione@crf.it
* Correspondence: a.concilio@cira.it; Tel.: +39-0823-62-3342

Abstract: The work at hand focuses on an adaptive system aimed at improving the soundproof performance of car door seals at specific working regimes (cruise), without interfering with the conventional open-closure operations. The idea addresses the necessity of increasing the seal effectiveness, jeopardized by aerodynamic actions more and more important as the speed increase, generating a pressure difference between the internal and the external filed, in the direction of opening the door. To recover this effect, an expanding mechanism was integrated within the seal cavity, driven by an SMA actuator. The material was activated (heated) by Joule effect; its compactness, intrinsic of smart materials, contributed to arrive to a final system characterized by a high level of integrability (expanding cells). In this paper, the development process is described together with the verification activity, aimed at proving the functionality of the realized device. Starting from the industrial requirements, the most appropriate solution was identified highlighting the working principle and the main design parameters involved. Then, the envisaged system was designed and its executive digital mock up (CAD) was released. Prototyping and laboratory validation showed the reliability of the numerical models and the associated predictions. On this basis, the integration task within the actual reference car was faced. To demonstrate the isolation effect of the proposed system, an experimental campaign was finally organized in an anechoic room, achieving significant results on the concept value.

Keywords: SMA actuators; smart isolation systems; soundproofing devices; active seals; expanding cells

---

1. Introduction

A critical aspect the automotive industry is currently facing is represented by the abatement of the environmental impact of vehicles, in compliance to more and more tightening regulations, encompassing, among the others, chemical and acoustic pollution aspects [1].

With the aim of meeting the environmental needs and, at the same time, consolidating their role in the market, the automotive companies are turning their attention to new technologies, characterized by an adequate level of maturity, to assure a quick and competitive diffusion on the open market. According to this trend, the car of the future will be electrified, autonomous, shared, connected and yearly updated [2].

Within this scenario, a critical role is played by the possibility of reducing weight[3], saving energy[4], abating chemical[5] and acoustic[6] emissions. A large number of subsystems are potentially involved: engines, aerodynamic shapes, gearboxes, cockpit, control unit settings, seals (for sound and water insulation), and so on.

Many research programs were funded in the last decades on these topics. Among the others one recalls: “Integrated Solutions for Noise and Vibration Control in Vehicles” (CO2NTROL), aiming at exploring the potentiality of integrated solutions for the control of noise and vibration in vehicles, to improve vehicle fuel efficiency and reduce their impact on the environment [7]; “Intelligent Materials

Preprints (www.preprints.org) | NOT PEER-REVIEWED | Posted: 29 October 2018 doi:10.20944/preprints201810.0693.v1

Peer-reviewed version available at *Actuators* **2018**, *7*, 88; doi:10.3390/act7040088

for Active Noise Reduction" (InMAR), focusing on new strategies and materials, to mitigate automotive environmental impact [8]; "Green City Car", aimed at developing and demonstrating integrated noise and vibration solutions, for a more efficient use of energy and weight savings [9]; "European competitiveness in commercial hybrid and automotive powertrains" (ECOCHAMPS), on power train efficiency improvement, weight reduction and cost abatement of hybrid vehicles, [10].

The scientific and industrial research focuses on several aspects, including:

- the assessment of predictive models and design strategies oriented to noise and vibration (to cite some examples, the dedicated models and development processes illustrated by Panda in [11]; the virtual car for sound and vibration prediction proposed by Genuit and Bray [12])
- the measurement of the radiated sound and related environmental impact (among the others, the investigation on the sound sources related to Germany train transportation network, performed by Werning et alii[13]; the assessment of dedicated strategies to measure of the noise radiated by specific automotive components, by Razak et alii[14]);
- the development and maturation of innovative materials with damping and insulation properties (e.g. shape memory alloys [15], magnetostrictive materials [16])
- the development and integration of noise and vibration control strategies (e.g. piezoelectric integrated solutions developed by Bein et alii in the above mentioned Project of Green City Car[17], the piezo shunted resonators described by Liao and Sodano in [18]18 and by Ciminello et alii [19], the SMA based architecture for changing the dynamic structural response developed by Ameduri et alii [20]).

The "Low Noise" Project (2012-2015), funded by the Italian Ministry of Education and Research, was conceived within this scenario, with the aim of reducing car noise and vibration fields, with the use of new solutions and novel, sustainable materials, which minimize the impact on weight and all the other characteristics that could have in turn a negative influence on consumption and emissions.

In detail, the activities targeted the reduction of acoustic sources that would be dominant in electric or hybrid vehicles, standing the lack of noise, typical of internal combustion motors. A systemic approach was necessary to achieve that objective, involving multiple vehicle functions, including door seal architectures.

The work at hand describes the tasks that were addressed within the Low Noise Project to develop an SMA-based active seals system and demonstrate its effectiveness in assuring established sound insulation levels. SMA technology was selected because of the experience, formerly matured in automotive applications, and the intrinsic compactness of the related devices, exhibiting high energy density, and high transmittable forces and deformations capability [21]. At first, moving from industrial requirements issued by the FGA Research Centre (CRF, Centro Ricerche FIAT), adaptive system specifications were generated. Secondly, a trade off analysis was performed, within which the technology solution was identified, as an axially expanding cell activated by a longitudinally contracting SMA wire. Design and modelling tasks were then accomplished to define detail system features (e.g. dimensions, materials, and so on), and identify foreseen operational performance (radial force generated, power supply). Prototyping phase was then addressed, defining all the executive parameters. Finally, an experimental campaign was organized, to verify the effective prototype ability in producing the necessary actions, and measure induced transmission abatement within an absorber chamber.

2. Seal adhesion problem and system specifications

Static aerodynamic loads acting on the wet car surface cause soundproof performance loss of the door seals. In fact, the specific car geometry produces and magnifies, at certain speeds, a lateral depression pushing the doors from the internal, reducing the seal adhesion strength. This phenomenon is schematized in Figure 1; a dedicated CFD analysis was conducted, showing a significant displacement field normal to the door surface, with some local maxima along its edges.

Preprints (www.preprints.org) | NOT PEER-REVIEWED | Posted: 29 October 2018 doi:10.20944/preprints201810.0693.v1

Peer-reviewed version available at *Actuators* **2018**, *7*, 88; doi:10.3390/act7040088

Figure 2 (left), illustrates a map of translations at the driver's door, generated by the aerodynamic forces and predicted through a FE modeling approach. Sealing performance depends on the adhesion strength, whose resultant (lift) is expressed as a function of the clearance, herein intended as the net distance between the door and the car cabin frame. Figure 2 (right), provides an example of this function, obtained through a non linear FE analysis taking into account the sealing compression. In that same plot, three regions are depicted: region 1) door closure beginning – sealing compression; region 2) door closed - nominal condition; region 3) effect of an additional compression due to an over-closure of the door. Dashed boxes represent the tolerance. To restore the soundproof performance, the gap at the door boundary has to be recovered. A solution is to expand the seals in order to recover the original adherence property.

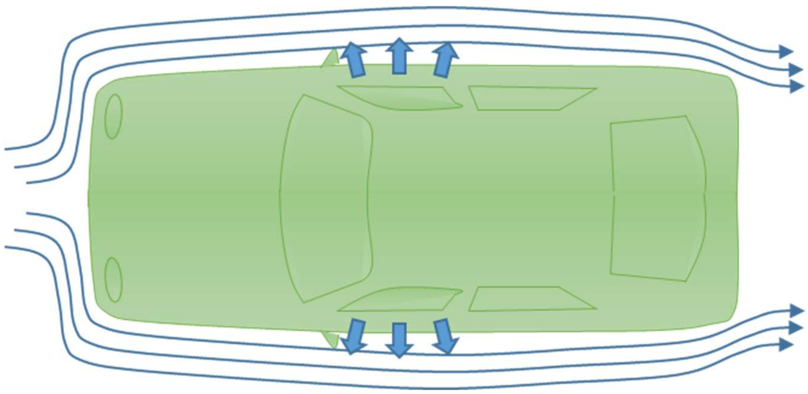

Figure 1. Qualitative representation of the phenomenon

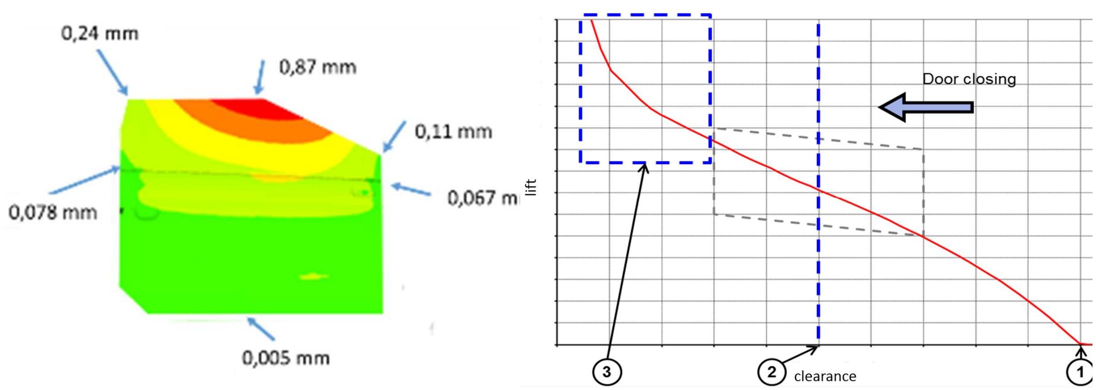

Figure 2. Generated displacement field (left) and sealing lift curve versus clearance(right)

Both the narrow space and the necessity of avoiding any interference with the door operation (opening and closing) make SMA actuators good candidates for compactness, and ease of use and installation. Moreover, the monolithic or quasi-monolithic nature of the concepts involving SMA materials generally leads to advantages in terms of reliability.

System automotive requirements involve several aspects:

- Recovering seals gap is lower than 1.0 mm (by engineering specs, derived from design constraints);
- Location zone is usually on the forward top corner edge, Figure 2;
- To be appreciable, SPL abatement shall be higher than 3dB over the frequency bands of interest;
- Temperature operational range shall be between - 50 and + 80 °C;
- Proposed system should be turned on during high-speed cruise segments, only; its full activation shall be completed within 1s;

- Electrical and thermal insulation shall be ensured between SMA system and the original seals;
- Power consumption should not exceed 5W per door.

3. Concept, integration and working phases

The concept herein presented aims at accomplishing the fundamental function of expanding the seal, to press it against the door and the related cabin frame. The system is made of three main components:

- A shell-like mechanical structure ("the cell"): it hosts a SMA active element inside and converts the action of that device into transversal displacements, pushing the seal rubber. The cell, a slender ellipsoid, is designed to fit the seal longitudinal cavity and transforms longitudinal into transversal actions.
- The SMA actuator, a wire element connected to cell edges at a certain pre-stress level and, equilibrated by the cell elastic reaction: heating by Joule's effect makes the SMA element to contract, compressing the cell longitudinally and inducing a transversal expansion (something equivalent to Poisson's effect).
- Mechanical, thermal and electrical interfaces: they assure an effective mechanical transmission between the wire and the cell, provide a thermal shield between the hot surface of the SMA, and the cell and the seal rubber, and limit electrical dispersions.

Figure 3 illustrates the cell working principle and the system integration phases. The cell structure is initially compressed as it passes from the condition (a, unloaded) to (b, pre-stressed). At that stage a non-stressed, full austenite SMA wire is inserted within the cell skeleton and constrained at the longitudinal edges (c). The system is then released and achieves its elastic equilibrium (d). It is remarked that SMA wire reaches a full martensite state in (d) if the structural pre-stress (b) is sufficient. The cell at this point is inserted within the seal cavity (e) and is ready to operate by heating (full austenite recovery – provided an adequate temperature is reached, wire shrinking and cell expansion, f). The abovementioned phases are placed along the stress-strain SMA diagram, Figure 3 (g). In that graph, SMA characteristic curves are reported at room (dashed) and at a given temperature (solid lines), high enough to enable complete phase transformation (martensite to austenite). In Figure 3 (g), another line is reported, representing the cell stress-strain characteristics, that is to say the applied axial force vs the produced axial strain. The intersections of that with the SMA characteristic curves identify the equilibrium states occurring during the cell installation and the system working phases. In other words, the reported lines allow recalling the set-up and operation steps. Unloaded cell is in the state (a). After compression it moves to state (b) when a SMA wire is installed (c). Cell elastic forces induce an extension of the SMA wire (achieving a full martensite transformation), while the structure recovers part of the imposed strain (d); in that condition, the system is installed in the seal (e) and ready to work. As SMA is heated, the operation point moves along the "elastic line", from a full martensite to a full austenite state.

Preprints (www.preprints.org) | NOT PEER-REVIEWED | Posted: 29 October 2018 doi:10.20944/preprints201810.0693.v1

Peer-reviewed version available at *Actuators* **2018**, *7*, 88; doi:10.3390/act7040088

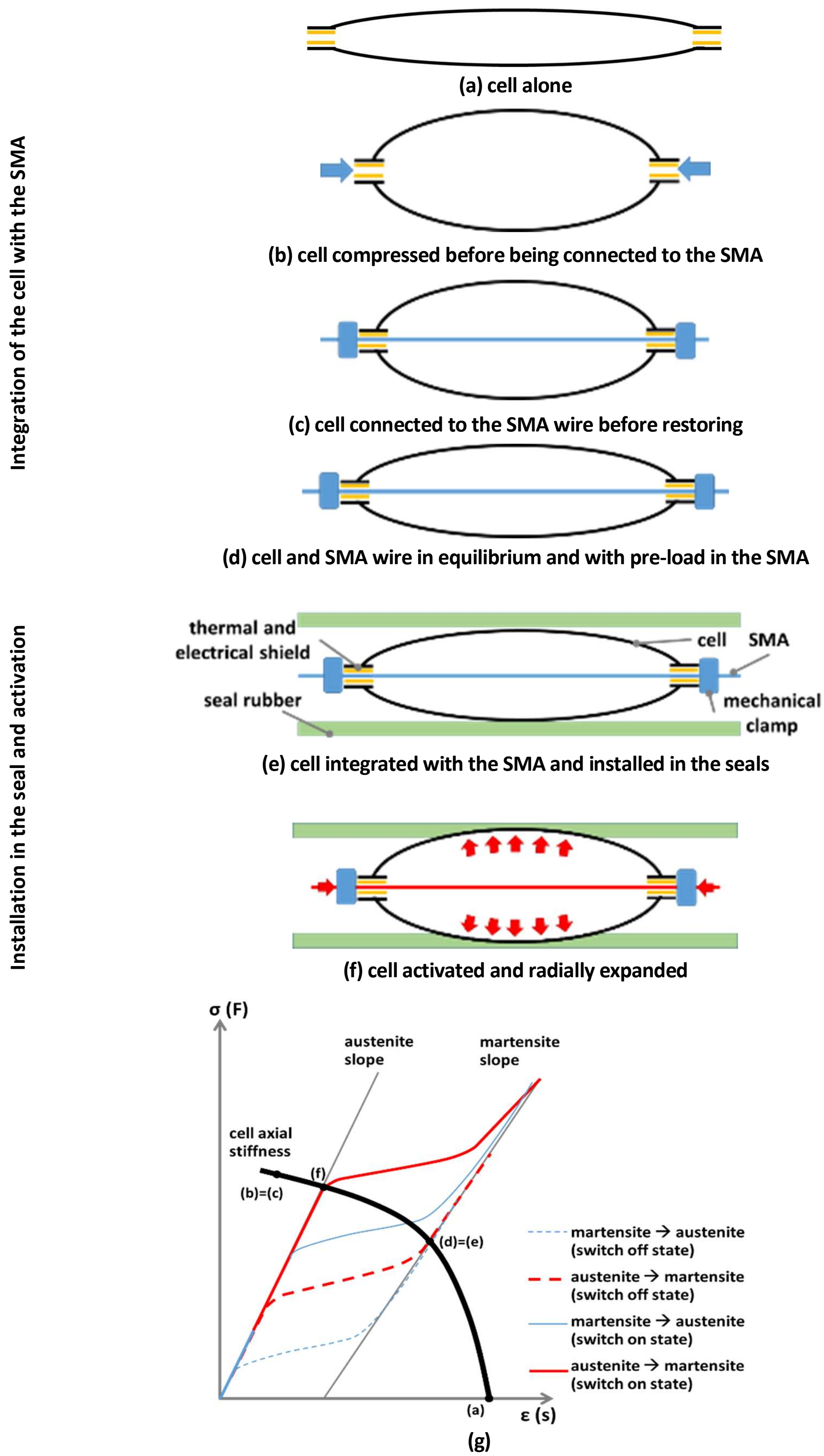

Figure 3. Integration process of the cell with the SMA wire (a – d), installation and activation within the seal (e – f), stress-strain curve comparison for the SMA and the cell vs the different integration phases (g).

Preprints (www.preprints.org) | NOT PEER-REVIEWED | Posted: 29 October 2018 doi:10.20944/preprints201810.0693.v1
Peer-reviewed version available at Actuators 2018, 7, 88; doi:10.3390/act7040088

4. System design

The selected design approach allows facing the cell and the SMA wire design, separately. In detail, cell material and geometry selection was driven by the following needs:

- Full integrability of the cell within the seal cavity, ensured in both on and off states;
- Guaranteeing a wide contact surface between cells and seal in order to maximize the interaction and distribute the load, uniformly;
- Establishing a sufficient length to reduce cell-seal interaction losses and minimize the side effect at the connection SMA-cell;
- Keeping the stress levels within the structure under a certain thresholds, to mitigate fatigue problems.

3.1. Cell modelling and sizing

Titanium alloy and plastic ABS materials were taken into account. The cell was designed with an ellipsoidal shape, optimized to magnify the expansion characteristics. The final configuration assured a good flexibility, producing a sufficient deformation field by a moderate level of applied stress. Longitudinal openings were dig in the original outline (Figure 4, left), arriving to a sort of three-arm arrangement, (Figure 4, right). Such configuration was shown to secure a suitable contact with both the door ring and frame, for any angular rotation within the seal.

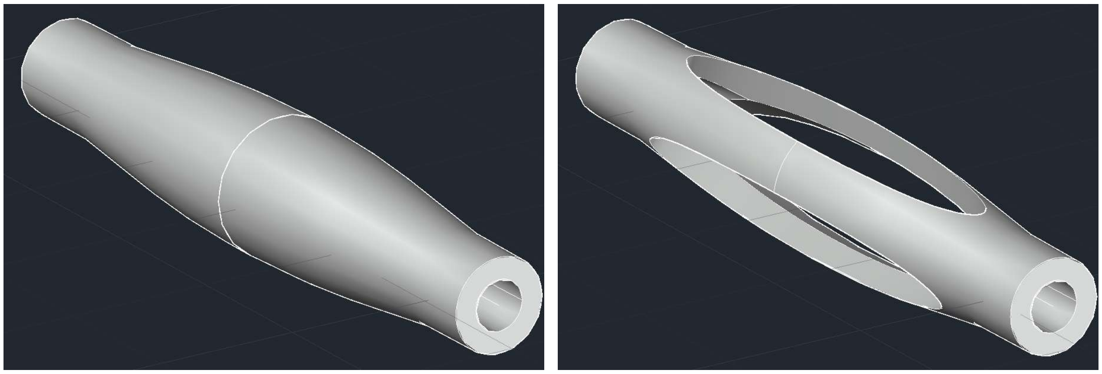

Figure 4. Ellipsoid geometry (left), three arms configuration (right).

Arm length, cross section area (thickness and width), and initial curvature were parameters taken into account in the established design process. The SMA-structural model described in [22] was implemented onto the system made of a single ellipsoid arm, in the way defined before, and the active wire. The structural element was assumed as a constant cross section beam, shaped like a sinusoid along its length (see Figure 5).

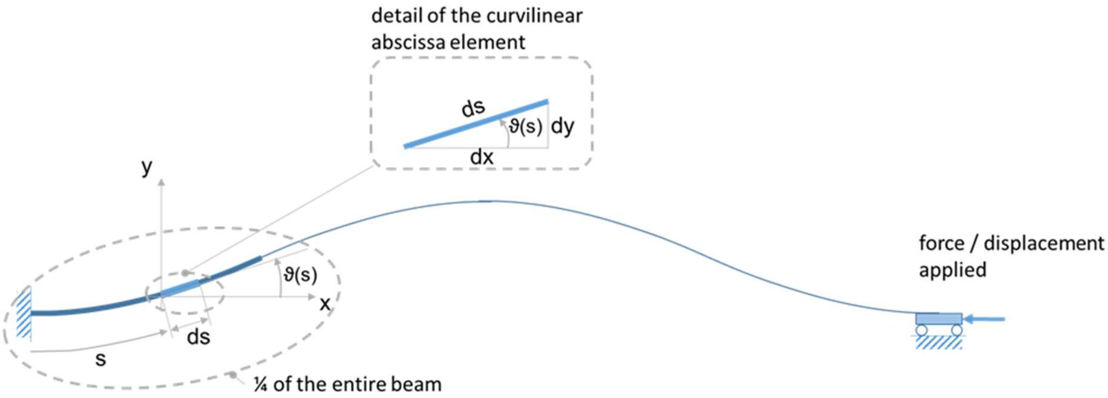

Figure 5. Structural scheme adopted for simulating the behavior of a single arm of the cell.

Preprints (www.preprints.org) | NOT PEER-REVIEWED | Posted: 29 October 2018 doi:10.20944/preprints201810.0693.v1

Peer-reviewed version available at *Actuators* **2018**, *7*, 88; doi:10.3390/act7040088

Its slope $\vartheta_0(s)$ was set in the range [0-π]. The local slope angle, $\vartheta(s)$, under an axial load, P, can be obtained numerically, by integrating the well-known equation, [23], versus the curvilinear abscissa, s:

$$EI\left(\frac{d^2\vartheta}{ds^2} - \frac{d^2\vartheta_0}{ds^2}\right) = -P\sin\vartheta \tag{1}$$

Under the hypothesis of small displacements and considering the problem symmetry, the equation may be integrated over just ¼ of the reference domain. The following boundary conditions can be assumed:

- $\vartheta(0) = 0$; (clamped at one edge);
- $d\vartheta/ds\ (L/4) = 0$; (curvature inversion at ¼ of the total length, L – inflection point).

Axial and the transversal displacement, Δx and Δy respectively, can be classically computed as:

$$\Delta x = \int_0^s \cos\vartheta(s)\, ds \tag{2}$$

$$\Delta y = \int_0^s \sin\vartheta(s)\, ds \tag{3}$$

being the elemental abscissa and ordinate, dx and dy, given by the multiplication of ds by the cosine and sine functions of the local slope, $\vartheta(s)$, respectively (see detail on the top of Figure 5).

The effect of the initial curvature (herein expressed as the ratio between the arm height at the middle span, h, and its overall length, L, shape coefficient) was at first investigated, Figure 6.

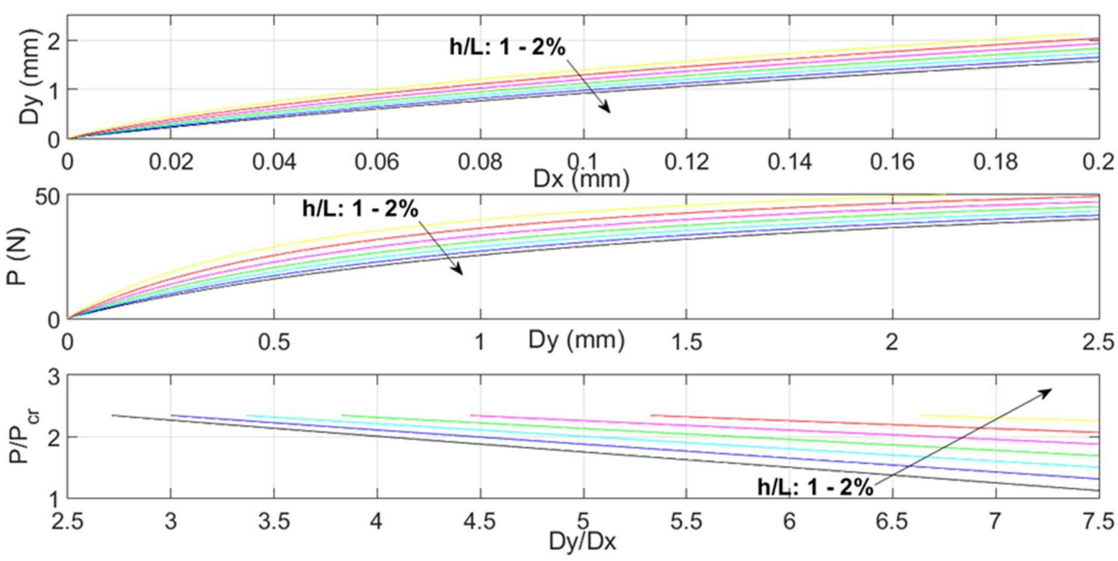

Figure 6. Transversal displacement (Dy), applied load (P) and load normalized with respect to critical buckling load (P/P_0) as a function of axial (Dx) and transversal (Dy) displacements, and their ratio (Dy/Dx), respectively. Curves parameterized vs the shape coefficient (h/L) in the range [1-2]%.

The three graphs highlight a marked nonlinear behavior of the cell structure, due also to de fact that the structure works in post-buckling condition. In fact, the first derivative of the transversal load vs transversal displacement curve is higher at the axis origin, while it becomes smoother and smoother for higher displacement value, clearly due to the structural instability effects. This kind of nonlinear relation is also evident in the bottom plot, where the ratio transversal vs axial displacement (Dy/Dx) magnifies for small values of the normalized load, higher than 1 for the post buckling

Preprints (www.preprints.org) | NOT PEER-REVIEWED | Posted: 29 October 2018 doi:10.20944/preprints201810.0693.v1

Peer-reviewed version available at *Actuators* **2018**, *7*, 88; doi:10.3390/act7040088

working modality. The shape coefficient, h/L, is shown to influence the arm, stiffness, reducing the load necessary to produce a certain displacement (axial or transversal).

Such results highlight the necessity of implementing a non-linear approach to face the advanced design of the cell element. To this aim, a dense FE model was realized by using tetrahedral elements. Model details are shown in Figure 7 and reported in Table 1. A 50 mm-long and 5mm-wide ABS cell, was considered a good compromise among the four basic requirements, aforementioned. The three arms are 1.5mm thick (radial direction) and 2.6mm wide (circumferential direction), average values.

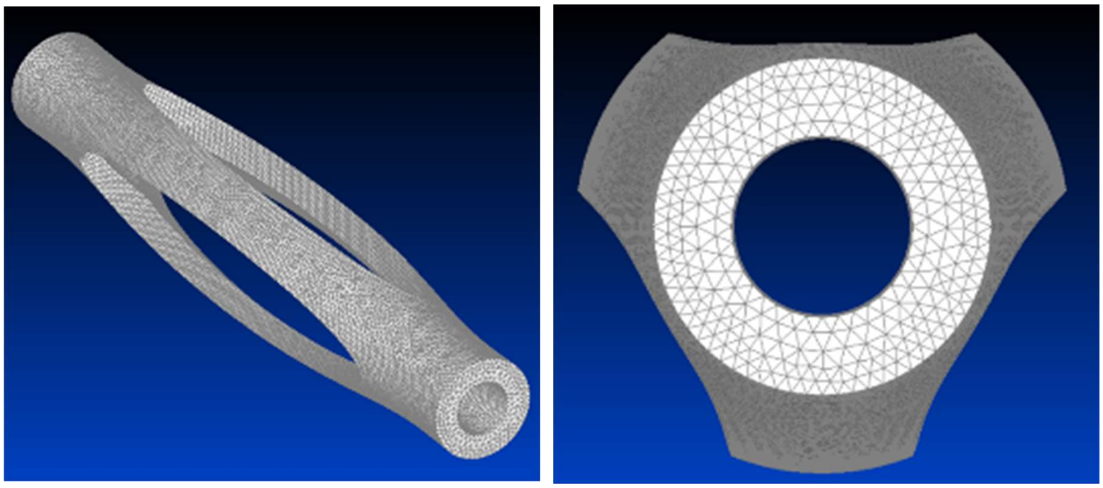

Figure 7. Finite Element Model of the cell body.

Length (mm)	Transversal size (mm)	Number of arms	Thickness (average) of the arms (mm)	Width (average) of the arms (mm)	Elements	Nodes	Young modulus (GPa)	Poisson modulus
50	5	3	1.5	2.6	175930	37947	2.3	0.32

Table 1. Main features of the finite element model of the cell.

FEM analyses provided a detailed description of the evolution of the mechanic parameters of the system. The first plot in Figure 8, left, illustrates the evolution of the Dy vs Dx, imposed to the cell by the SMA wire action. Slope change (decrease) of the curve is evident and in good agreement with the theoretical model and coherent with the structural behavior, working in the instability region. Such result is confirmed by the evident decrease of the axial force vs axial displacement ratio, Figure 8, right. There, a “knee” at a 0.2 mm axial displacement splits the graph into two regions: one, where the cell appears stiffer and another where it offers a still growing axial reaction but with a more moderate and decreasing slope (post buckling region).

Preprints (www.preprints.org) | NOT PEER-REVIEWED | Posted: 29 October 2018 doi:10.20944/preprints201810.0693.v1

Peer-reviewed version available at Actuators 2018, 7, 88; doi:10.3390/act7040088

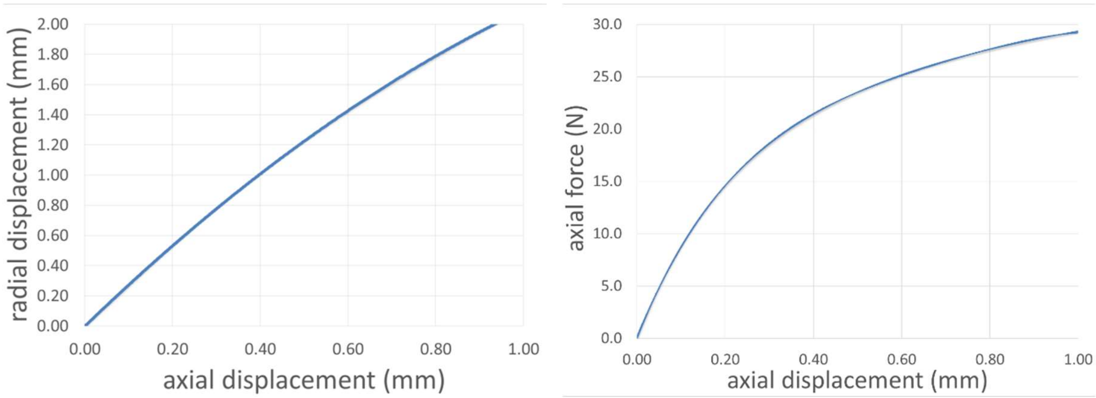

Figure 8. Cell radial displacement (left) and axial force (right) versus the axial displacement.

A stress analysis was finally performed to verify the cell integrity in the most severe condition (2 mm max radial displacement, Figure 8, left) and highlight the most critical zones. Von Mises strain map is shown in Figure 9; some local maxima at the middle of the arms are evident. Other maxima are visible at the extremities, where however boundary and application forces effects are clearly present. Deformation values attain about 1.85% (18500 με), corresponding to 42.5 MPa stress, well below the ABS ultimate strength (66.7 MPa).

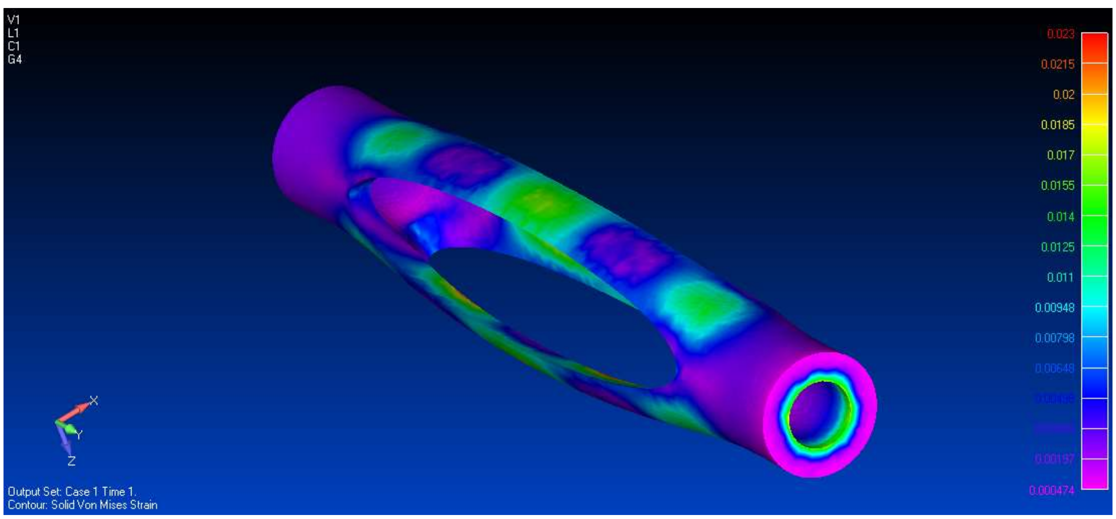

Figure 9. Von Mises strain map for the maximum transversal displacement (2 mm).

3.2. SMA wire modelling and integration within the cell

Having frozen the cell design, SMA element features definition and cell body integration issues were faced. Shape memory alloys properties and wire cross section should have been defined in compliance with the general system requirements with the specific target of exploiting SMA contraction and recovery capability, in order to maximise the cell expansion/contraction cycle. In this case, the implemented design strategy was based on the definition of an analytical model able to reproduce the plot, reported in Figure 3, bottom. This curve would have been then overlapped to the cell elastic curve, Figure 8, right. To this target, the model described in [24] was adopted. For the sake of clearness, the equations describing the forward (austenite → martensite) transformation are reported, explicating the relation among martensite concentration, ξ, stress field, and temperature.

$$\xi^{fwd} = \frac{[\sigma_{SMA}H + \sigma_{SMA}^2 \Delta S_{33} + f^{fwd}(T)]}{\varrho \Delta s_0 (M_{s0} - M_{f0})} \quad (4)$$

Preprints (www.preprints.org) | NOT PEER-REVIEWED | Posted: 29 October 2018 doi:10.20944/preprints201810.0693.v1

Peer-reviewed version available at Actuators 2018, 7, 88; doi:10.3390/act7040088

where ξ^{fwd}, σ_{SMA}, H, ΔS_{33}, Δs_0, ϱ, M_{s0}, M_{f0} are the martensite concentration, the current stress within the SMA wire, the maximum recoverable strain, the compliant matrix element in the axial direction of the wire, the entropy change between austenite and martensite phases, the SMA density, and the 0-stress martensite transformation start and finish temperatures, respectively. Finally, the function $f^{fwd}(T)$ is given by:

$$f^{fwd}(T) = \varrho\Delta c\left[(T - T_0) - T\ln\left(\frac{T}{T_0}\right)\right] + \varrho\Delta s_0(T - M_{s0}) \quad (5)$$

being T and $T_0$the current and reference temperatures, and Δc the change of the specific heat coefficients between austenite and martensite phases. To complete the representation of the shape memory alloy state, the following equation shall be considered:

$$\varepsilon_{33} = \frac{1}{E_A + \xi^{fwd}(E_M - E_A)}\sigma_{33} + H\xi^{fwd} + \alpha(T - T_0) \quad (6)$$

expressing the strain as a function of the just mentioned martensite concentration, ξ^{fwd}, the stress along the wire direction, σ_{33}, and the expansion thermal coefficient, α. E_M and $E_A$are the martensite and austenite phases Young's moduli, respectively. The above and the converse transformation (martensite → austenite) equations were used to trace the SMA stress-strain curves for both loading and unloading cycles at different temperatures. This model allowed defining the most significant SMA parameters, as reported in Table 2.

Wire length (mm)	Diameter (mm)	Young modulus (GPa)		Poisson modulus	Transformation temperatures (°C)				Maximum recoverable strain (%)
		E_M	E_A		M_{f0}	M_{s0}	A_{s0}	A_{f0}	
50	0.25	15	25	0.32	-48.0	1.0	-17.0	17.0	2.3

Table 2. Features of the SMA active element.

The diagram in Figure 10 represents the working domain of the assessed system, in terms of structural (cell) and SMA device behaviour. The cell stiffness curve (dashed line) is referred to an axes system with the x reversed with respect to the SMA reference. The reason is that a structural contraction corresponds to an alloy expansion and vice-versa. For the sake of clearness, only five full SMA cycles are therein represented: a grey scale is used to distinguish among room (darker) and higher temperatures (lighter and lighter). The intersections among the cell stiffness curve and the bottom segment of the transformation cycle (martensite → austenite), highlighted with circular markers, give the working points at growing temperature values. Max temperature was 170 °C, enabling the full transformation of the considered alloy. In the tests, that value was handled through adequate thermal shield insulations. Produced axial displacement is reported in Figure 11. At the highest car operational temperature, 80 °C, no activation occurs.

Preprints (www.preprints.org) | NOT PEER-REVIEWED | Posted: 29 October 2018 doi:10.20944/preprints201810.0693.v1

Peer-reviewed version available at Actuators 2018, 7, 88; doi:10.3390/act7040088

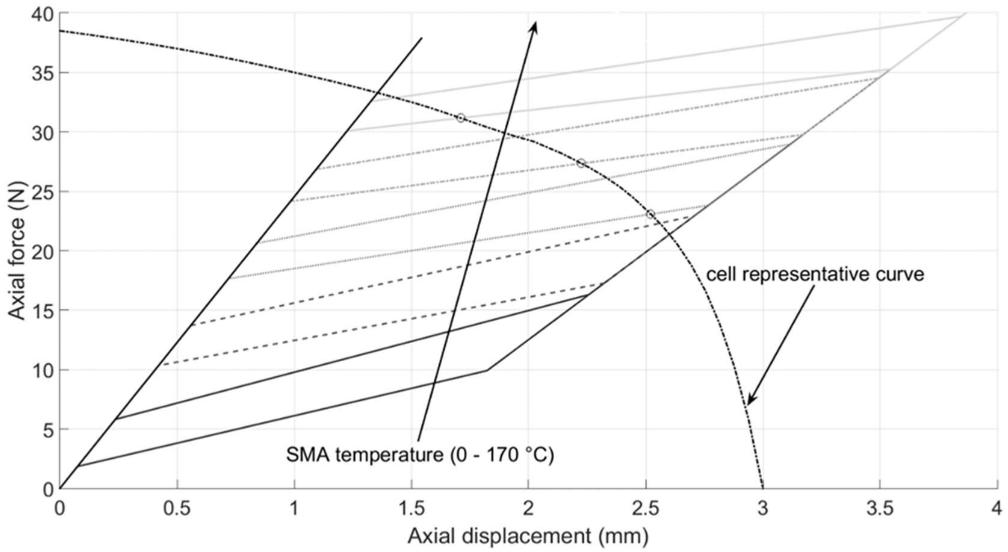

Figure 10. Operational points of the expanding cell.

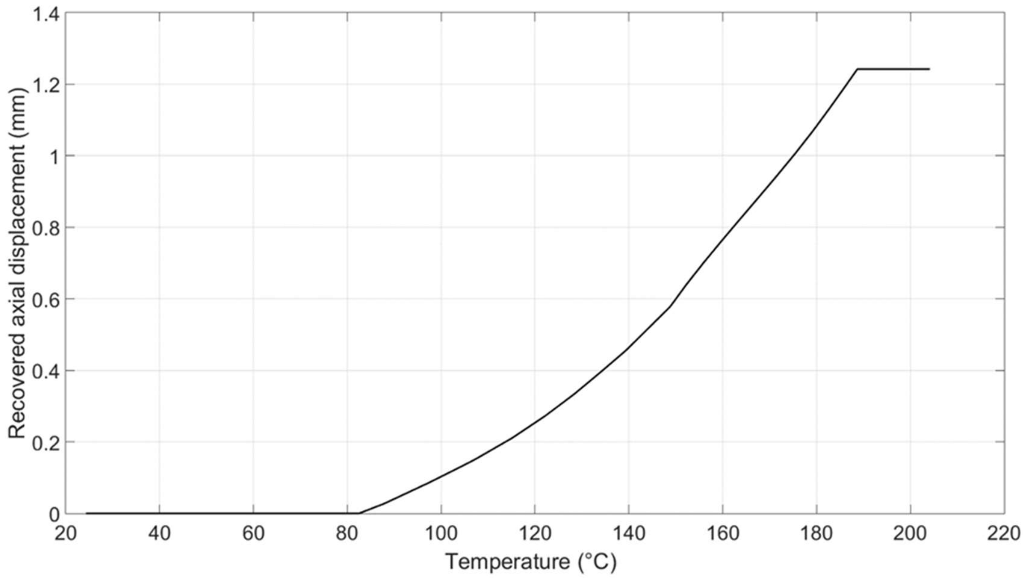

Figure 11. Axial displacement versus temperature.

4. Prototyping and validation

The design phase described above led to produce executive drawings of the prototype of a cell, addressed to laboratory functionality and mechanical validation. A 3D ABS printer was used to fabricate the elements. The prototype was used to estimate the actual structural properties and validate the proposed theoretical and numerical models. In Figure 12, a photo of the real cell is presented. One of the three arms was integrated with a strain gage on the middle span, to acquire deformation levels at the most critical zone, according to the numerical predictions shown in Figure 9. A dedicated test campaign was organised with the aim of acquiring the most significant mechanical parameters of the integrated system. A specific set-up hosting the cell was prepared, outlined in Figure 13 and shown in Figure 14. It was made of the following main components:

- The acquisition system Cronos PL8, handling strain gages, LVDT and load sensors signal;
- A mechanical press, to apply axial loads to the cell;
- A strain gage;

Peer-reviewed version available at Actuators 2018, 7, 88; doi:10.3390/act7040088

- An LVDT sensor, for measuring the axial displacement (compression) of the cell;
- A force sensor, to acquire the effective axial load (press action).

A summary of the outcomes of the experimental campaign is reported in Figure 15. A good agreement with the numerical predictions was found, in terms of applied axial load vs strain, measured at the arm center.

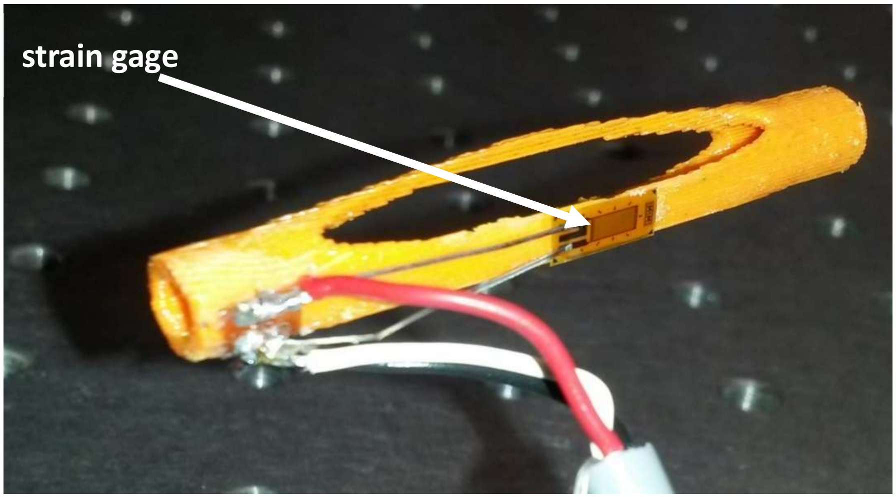

Figure 12. Prototype of a single cell.

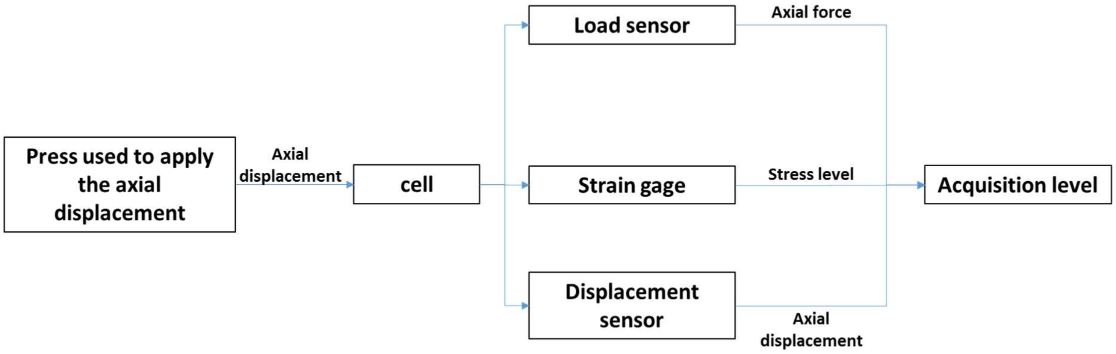

Figure 13. Scheme of the setup used for laboratory validation.

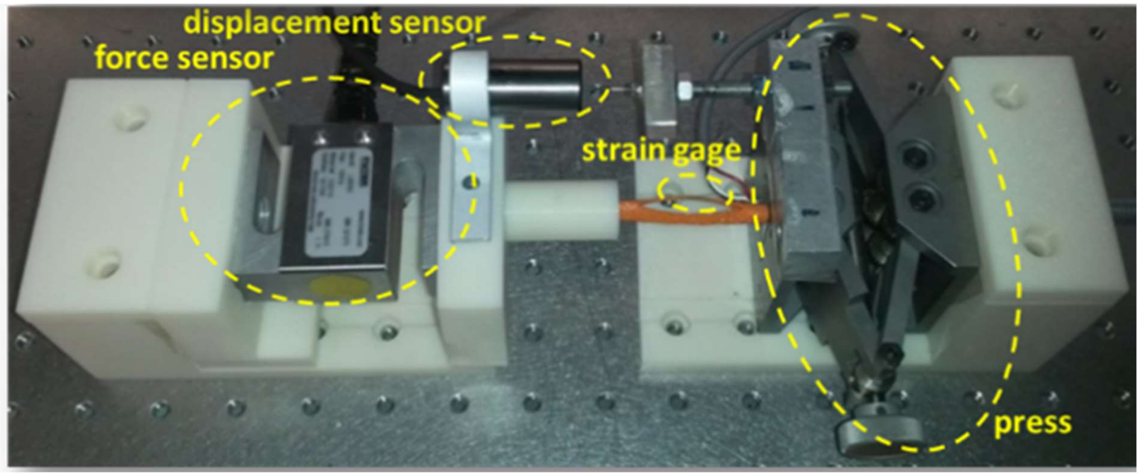

Figure 14. Experimental setup for laboratory tests.

Preprints (www.preprints.org) | NOT PEER-REVIEWED | Posted: 29 October 2018 doi:10.20944/preprints201810.0693.v1

Peer-reviewed version available at *Actuators* **2018**, *7*, 88; doi:10.3390/act7040088

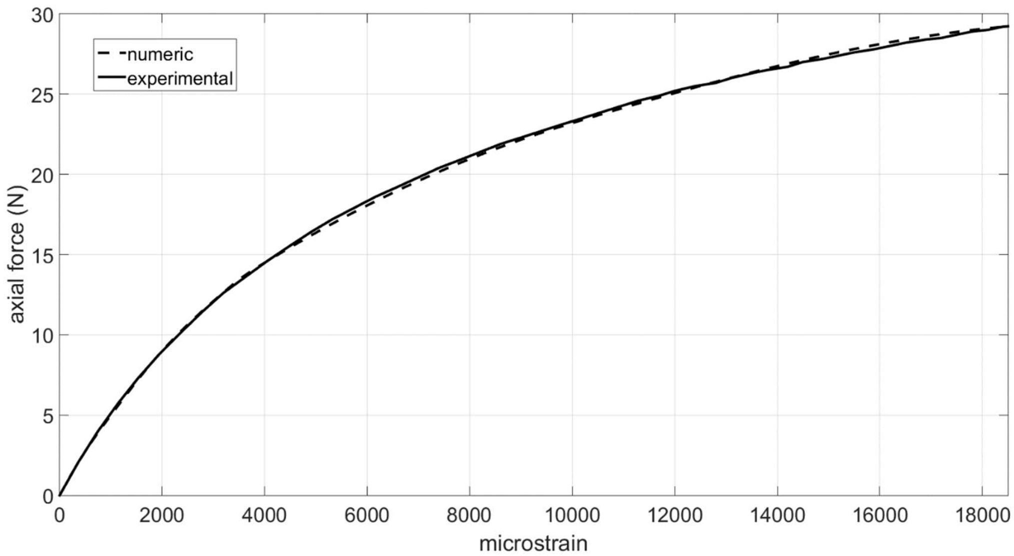

Figure 15. Axial load vs strain on the arms, numerical vs experimental.

A second prototype was then manufactured, made of three serial cells, relatively rotated by 60 deg for a better distribution of the actions on the seal. The length of a 3-cell device, like the one herein presented, corresponds to a specific critical door edge zone dimension (door upper corner, resulting the one characterised by the maximum separation in the range of interest, Figure 2). The digital mock up (DMU) provides some detail of the proposed system, Figure 16, top. The idea of grouping three cells is driven by the need of achieving an augmented compactness level. A single wire with two connections, clamped by hexagonal caps at the extremities, can activate the cluster. An established pre-load is assured by a screw system at one edge: spacer, in Figure 16, bottom. A detail of this tensioner is provided on the bottom left of the same picture: the SMA wire passes through a threaded hole. An external cylinder, the spacer, contains the wire-core assy. A tightening nut is screwed around the core to press the spacer against the cell. Finally, in the bottom right schematics, the Teflon cylinders for thermally protecting the cell from wire heating, are shown.

Preprints (www.preprints.org) | NOT PEER-REVIEWED | Posted: 29 October 2018 doi:10.20944/preprints201810.0693.v1
Peer-reviewed version available at Actuators 2018, 7, 88; doi:10.3390/act7040088

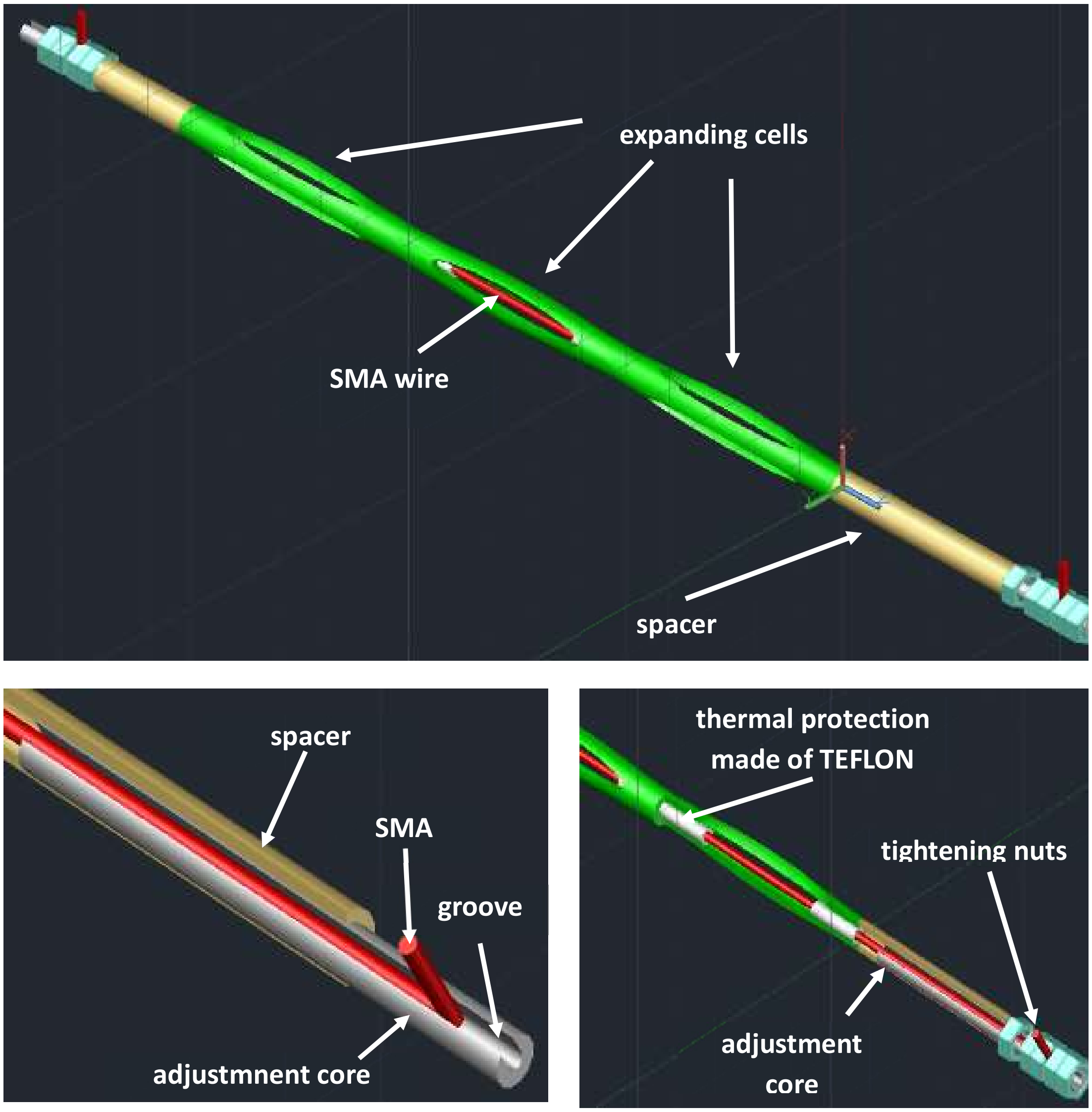

Figure 16. Digital mock up of a cluster of three cells integrated with a SMA wire.

A picture of the realized prototype, is illustrated in **Figure 17**. One of the cell arms was integrated with an FBG strain sensor placed at its mid-span, with a 1.2pm/με sensitivity coefficient. In order to ensure a reliable bonding of the sensible element over the irregular surface of the item, withstanding both large strain and temperature ranges during tens of cycles, an 80μm-diameter polyimide-coated fibre and a high-viscosity epoxy resin M-Bond GA-2 (6% max strain after 48h RT curing) were selected. Due to high-viscosity GA-2 acted as a filler, making a smooth surface. The FBG was interrogated by a Micron Optics Interrogator (MOI) SM-130, at 10Hz sample rate. Finally, a K-type thermocouple mounted on the wire surface, acquired the temperature during the complete test campaign. Functionality tests were then carried out, to verify the SMA wire ability to transmit proper transversal displacements.

Preprints (www.preprints.org) | NOT PEER-REVIEWED | Posted: 29 October 2018 doi:10.20944/preprints201810.0693.v1

Peer-reviewed version available at Actuators 2018, 7, 88; doi:10.3390/act7040088

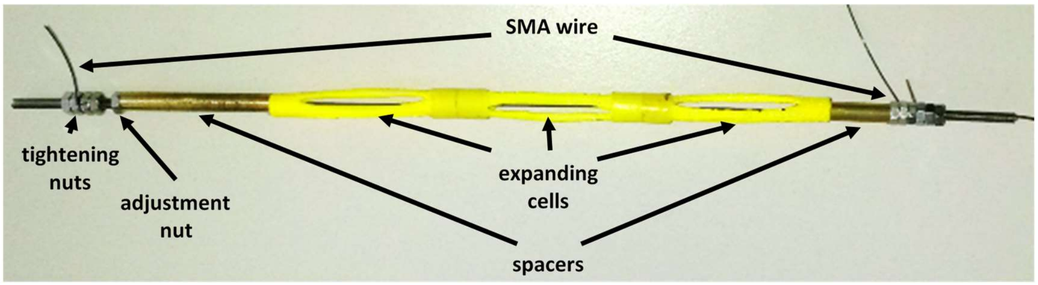

Figure 17. Three cells prototype, integrated with the SMA wire.

A stabilized current generator (DELTA Elektronica ES 030-10, 6.1 W max power) was connected to the SMA wire. A photo of the experimental setup is shown in Figure 18. The generator was driven on and off by a logical signal, assuring a 10% duty cycle with a 60sec period of excitation (that is to say 10 s on and 50 s off). The achieved cell expansion is compared with the basic state in Figure 19. The arms exhibited a 1.3mm radial displacement. In the horizontal plane, the global expansion projection achieved about 2.0mm. Before undergoing the tests, SMA wires were suitably trained to assess their recovery performance, in order to assure in turn adequate levels of repeatability. Strain evolution vs activation temperature is reported in Figure 20 for 15 cycles, till convergence.

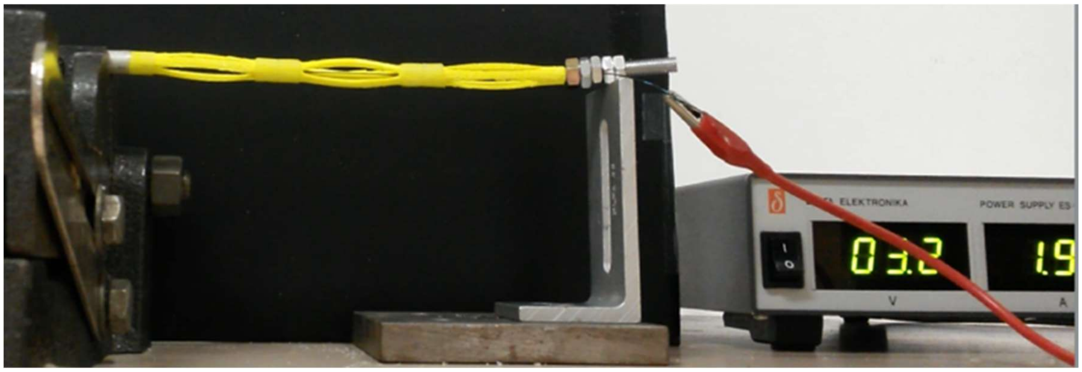

Figure 18. Setup for estimating the transversal displacement produced by the SMA wire.

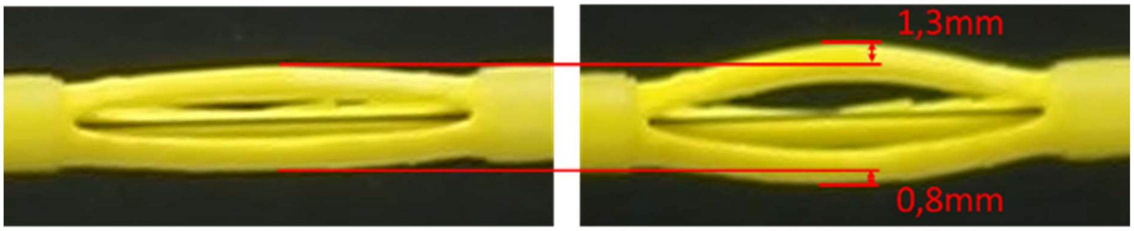

Figure 19. Cell functionality: fully activated (right), no active (left).

Preprints (www.preprints.org) | NOT PEER-REVIEWED | Posted: 29 October 2018 doi:10.20944/preprints201810.0693.v1

Peer-reviewed version available at Actuators 2018, 7, 88; doi:10.3390/act7040088

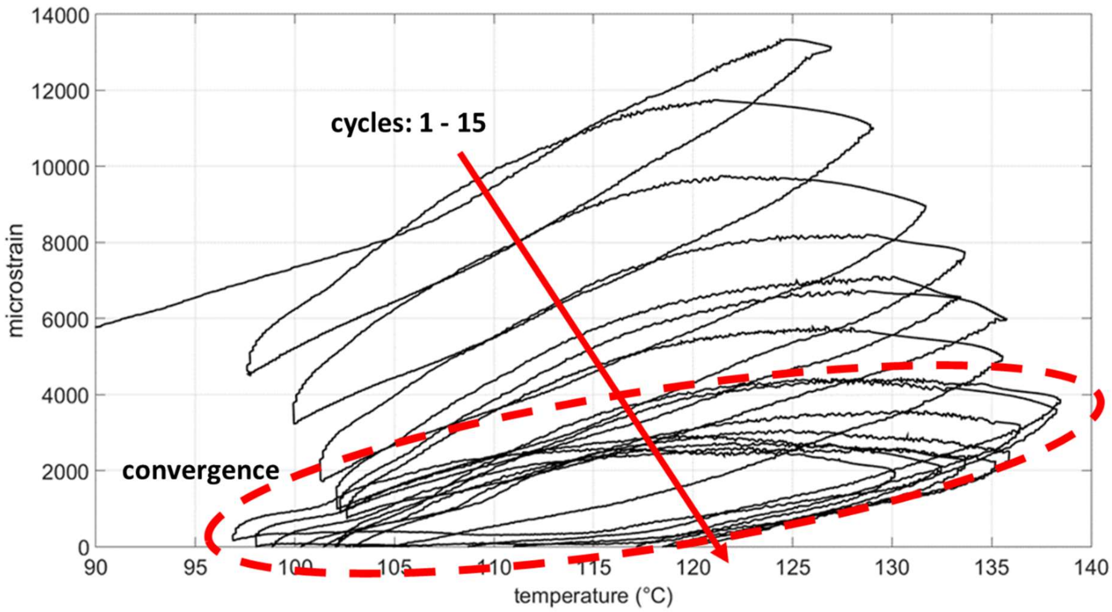

Figure 20. Time correlation between SMA temperature and cells strain.

5. Installation and acoustic tests

After proving the mechanical functionality of the system, its integration into the driver's door was addressed, within an actual car, available for the experimental campaign. To this purpose, two small hollows were drilled in the door seal, downstream and upstream the zone labelled "corner of insertion" in Figure 21, on the top. The power cords were connected to the cell cluster through the hollows, running from the bottom to the top; there, they were pulled out to place the cell cluster on the targeted region. After the integration, a dedicated setup was prepared for measuring the system soundproof performance. The test car was moved into the hemi-anechoic room of CIRA (5.5x5.3x5.0 m ≈ 145 m^3 – 90 Hz cut-off frequency [25]). The effect produced by the static aerodynamic action on the door was simulated through a screw system mounted on the door frame, modulating the separation (gap) between the door and the main body. To characterize the performance improvement of the sound insulation system due to the SMA-based device, a dedicated setup was assessed, whose schematic is reported in Figure 23. The driver's seat head restraint was equipped with two microphones (PCB type 377B02) to measure the sound field close to the driver's ears. The external noise was generated by a high-power omnidirectional loudspeaker (Bruel & Kjaer type 4292-L) installed outside, about 1 meter away from the driver's door. A reference microphone was mounted close to the driver's window in order to tune the external noise and achieve the required SPL. A SCADAS III LMS acquisition system was used to drive the source and acquire microphone signals. A signal generator, monitored by an oscilloscope, was used to drive the current stabilized power supply (model DELTA Elektronica ES 030-10) for the SMA system activation. An overview of the entire mock-up mounted in the hemi-anechoic room is shown in Figure 24.

Preprints (www.preprints.org) | NOT PEER-REVIEWED | Posted: 29 October 2018 doi:10.20944/preprints201810.0693.v1

Peer-reviewed version available at Actuators 2018, 7, 88; doi:10.3390/act7040088

Figure 21. Integration of the SMA adaptive system within the door seal.

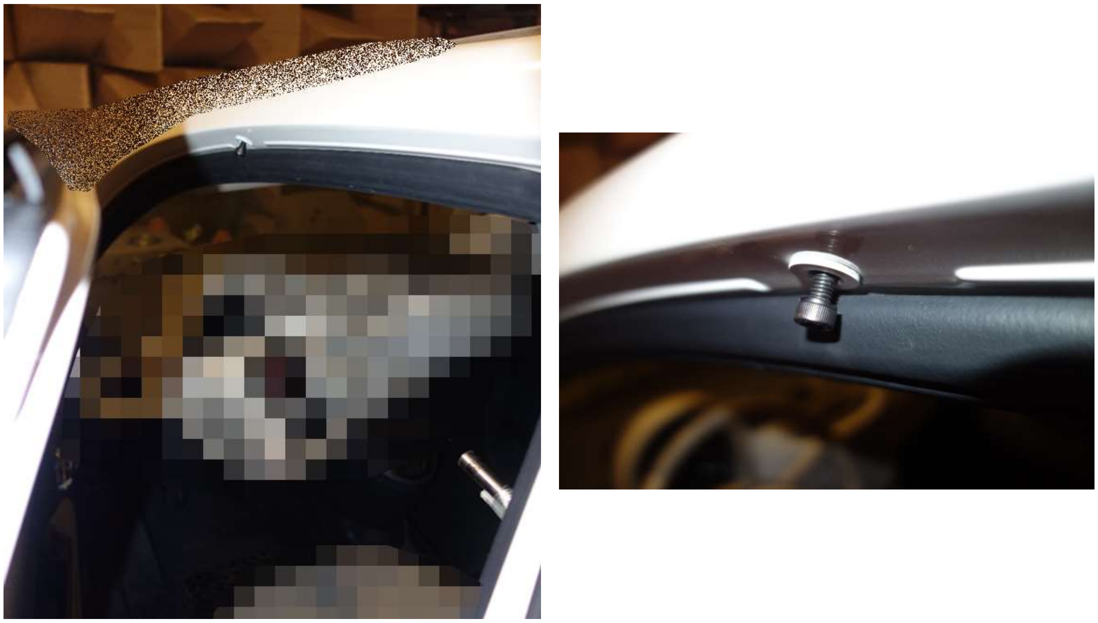

Figure 22. Screw system used to generate a gap between the seal and the door frame.

Preprints (www.preprints.org) | NOT PEER-REVIEWED | Posted: 29 October 2018 doi:10.20944/preprints201810.0693.v1

Peer-reviewed version available at Actuators 2018, 7, 88; doi:10.3390/act7040088

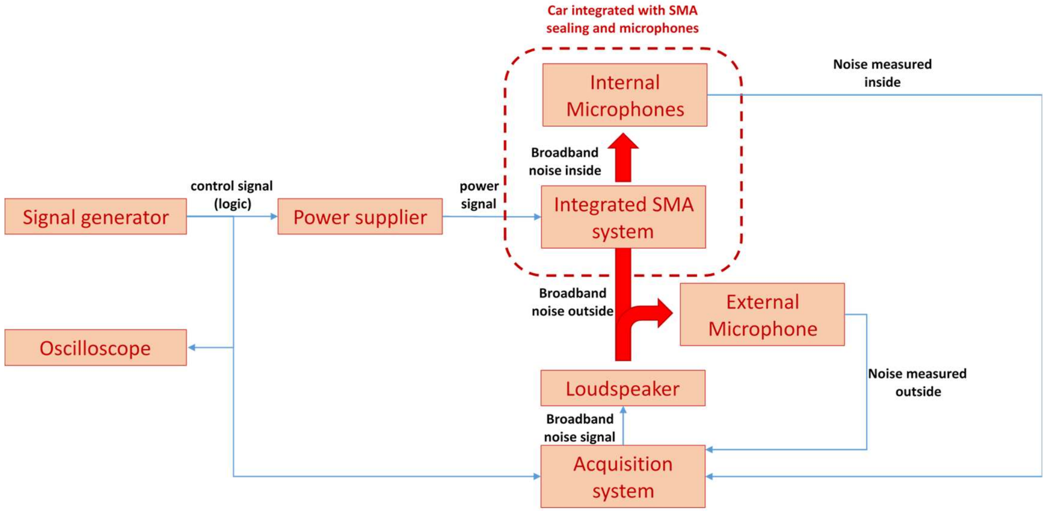

Figure 23. Schematics of the setup for acoustic characterization.

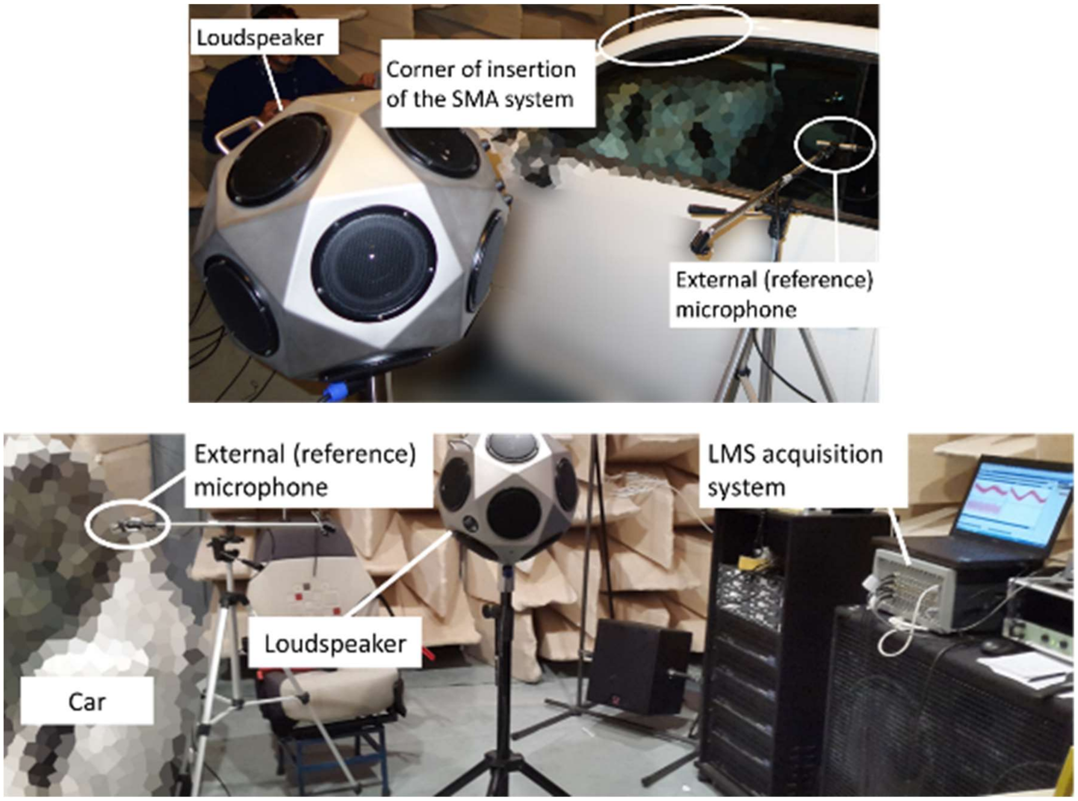

Figure 24. Experimental mock up.

The tests were executed for 5 gap sizes, ranging from 0.10 to 2.15mm. This range, suitably higher than the max expected gap (0.30mm), was chosen to prove the system functionality in operative and off-design conditions, e.g. due to an undesired seal damage. A linear sine sweep signal (chirp, 50-8000 Hz) was used to excite the vibroacoustic system. The Sound Pressure Level (SPL) was acquired with the SMA system off. The SPL difference between that value and what recorded at the external of the cabin is reported in Figure 25, for the octave bands ranging from the 3rd to the 8th and for different gap values. As therein shown, the transmitted noise is generally higher for the octave bands N.3, 4 and 6, whatever is the opening value. The effects due to the SMA device activation were then

Preprints (www.preprints.org) | NOT PEER-REVIEWED | Posted: 29 October 2018 doi:10.20944/preprints201810.0693.v1

Peer-reviewed version available at Actuators 2018, 7, 88; doi:10.3390/act7040088

measured, Figure 26. Those values refer to an average process over 20 cycles (microphone signals). The active cell required a power level of 6W for each cycle, lasting 60s. After every activation period, the system was switched off for 120s, letting the complete system to relax and move back to the original state (cooling and non-activated strain field restoring processes). Negative and positive values in Figure 26 indicate SPL attenuation or amplification, respectively. A significant abatement results for the minimum gap investigated (0.10 mm), as proved by the good attenuation at the 5th, 6th, 7th and 8th octave bands. A similar behaviour can be observed for the 0.5mm gap: in this case, the SPL reduction is even higher (at the 6th octave band). A more modest abatement is observed for larger gaps (1.85 and 2.15 mm) and in any case for lower than the 6th band.

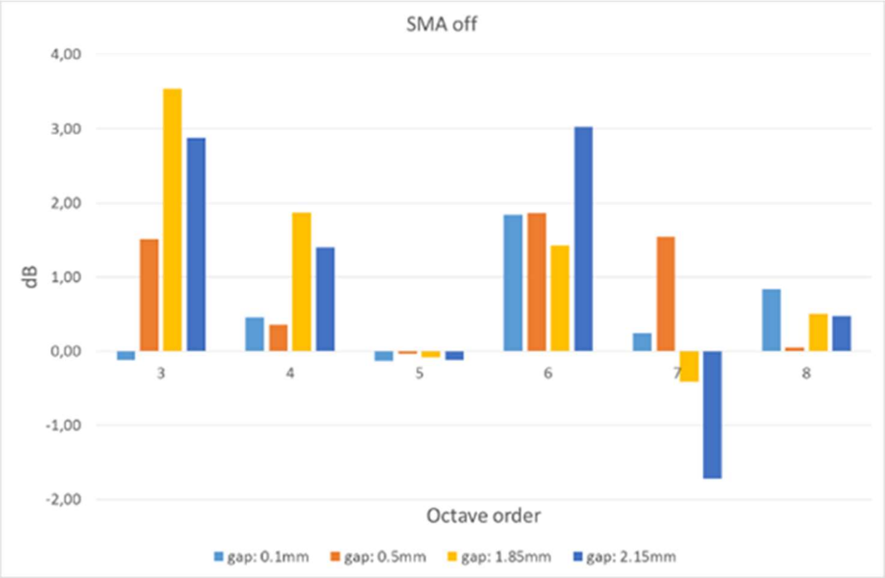

Figure 25. Sound pressure level without activating the SMA system.

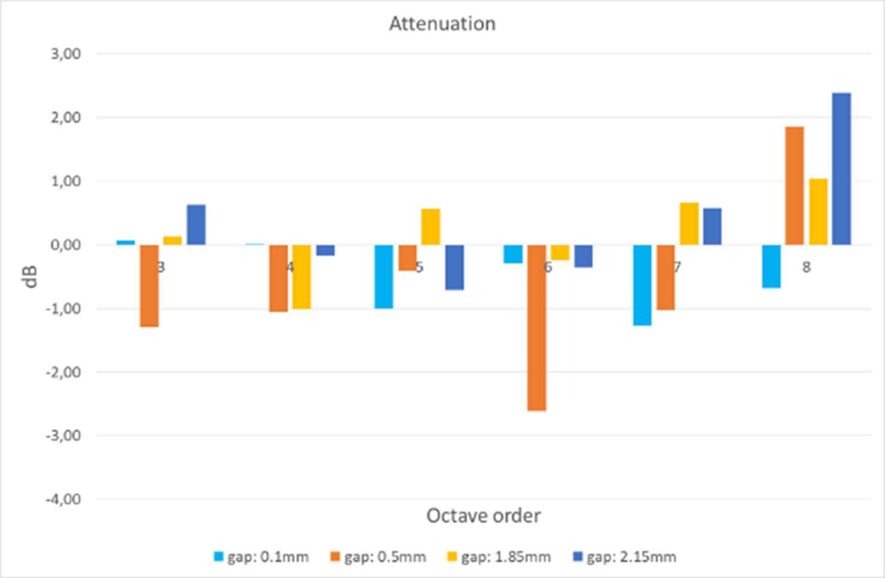

Figure 26. Sound pressure level abatement due to the activation of the SMA system.

Peer-reviewed version available at *Actuators* **2018**, *7*, 88; doi:10.3390/act7040088

6. Conclusions and further steps

In the present work, the development of a system for improving the soundproof performance of the car door insulation was presented. The system, based on SMA technology, is made of expanding cells integrated within the seal cavity. By activating the SMA material, a transversal expansion of the cell is enforced, with the final effect of increasing the net volume occupied by the acoustic protection and recovering doorframe leakages, caused by the action of aerodynamic forces, at specific regimes. Moving from industrial requirements, the system was preliminarily identified and its specific functionality levels (transversal actions transmission) was qualitatively described by means of a devoted theoretical model. That analytical representation was coupled with a 1D SMA model, developed by the authors and integrated with a well-established SMA constitutive law. After having verified the nonlinear behaviour of the system, the advanced design was carried out. A detailed FE model was prepared to this scope. A nonlinear static analysis was implemented, providing detailed information on the stress distribution and getting precious information on possible improvements. After this step, the experimental validation task was faced. At first, a laboratory setup was prepared, with the aim of relating the functional parameters of the isolated cell structure. A relation was found among the axial force applied to the cell, and the induced axial and transversal displacements. Results showed a good agreement with the numerical predictions. After this first validation, the SMA wire was integrated in the cell and the system functionality was tested for several activation-deactivation cycles. The soundproof performance of the developed system was finally verified. To this scope, it was integrated within the car after having organised a dedicated setup within the hemi anechoic room at CIRA. The tests, again run for several cycles, proved the architecture capability for different gap values, imposed through a dedicated screw system. Standing the performed activities, the herein presented concept was developed till TRL=4 and is considered a promising technology. Other steps are planned to further enhance its TRL. Among the others, fatigue and aging behaviour should be investigated, deriving from continued use and temperature changes; such aspects have impacts on several design steps, ranging from materials selection to the optimisation process.

Acknowledgments: The activities are part of and received funding by the National Project LowNoise ("Nuove tecnologie e materiali per l'abbattimento del rumore degli autoveicoli", PON_01_01878, starting date: 01/06/2012, duration: 36 months).

Author Contributions: conceptualization, A. Concilio, S. Ameduri; methodology, S. Ameduri; software, S. Ameduri; validation, V. Quaranta, S. Ameduri, M. Ciminello; formal analysis, S. Ameduri, A. Concilio; investigation, S. Ameduri, M. Ciminello; resources, A. Brindisi; data curation, S. Ameduri, V. Quaranta; writing—original draft preparation, S. Ameduri; writing—review and editing, A. Concilio, S. Ameduri; visualization, S. Ameduri; supervision, M. Brandizzi; project administration, V. Quaranta; funding acquisition, M. Brandizzi.

Conflicts of Interest: The authors declare no conflict of interest.

References

1. Hooftman, N., Messagie, M., Van Mierlo, J., Coosemans, T. A review of the European passenger car regulations – Real driving emissions vs local air quality, *Renewable and Sustainable Energy Reviews* **2018**, *86*, pp. 1–21, https://doi.org/10.1016/j.rser.2018.01.012.
2. Five trends transforming the Automotive Industry. Available online: www.pwc.com/auto (accessed on 26 10 2018)
3. Yadav, P., Shinde, A., Gangurde, Y., Patil, P. Review on Weight Reduction in Automobile, *Intern. J. of Advanced Technologies in Engineering and Science* **2016**, *4*, 1, pp. 478-483, ISNN 2348-7550.
4. Simpkin, R., D'Ambrosio, C., Simonsson, J., Abele, M, Ferrè, A., Rollenitz, L., Estrada Vasquez, R., Boldea, I., Scridon, S., Energy Efficient Vehicles for Road Transport, *Procedia - Social and Behavioral Sciences* **2018**, *48*, pp. 3613 – 3621, https://doi.org/10.1016/j.sbspro.2012.06.1324

5. Inomata, S., Yamada, H., Tanimoto, H. Investigation on VOC Emissions from Automobile Sources by Means of Online Mass Spectrometry, *Current Pollution Reports* **2016,** *2*, pp. 188–199, DOI 10.1007/s40726-016-0032-6.

6. Patil, A. V., Kumar, B., Barjibhe, R. B. An Extensive Review on the Use of Acoustic Emission Technique for Continuous Monitoring, *Int. Research J. of Engineering and Technology* **2016,** *3*, 5, pp. 137-140, ISSN: 2395 - 0056.

7. Integrated Solutions for Noise and Vibration Control in Vehicles. Available online: https://cordis.europa.eu /project/rcn/92595_en.html (accessed on 26 10 2018).

8. Intelligent Materials for Active Noise Reduction. Available online: https://cordis.europa.eu /result/rcn/ 47813_en.html (accessed on 26 10 2018)

9. Green City Car. Available online: https://fp7-co2ntrol.eu (accessed on 26 10 2018).

10. Ecochamps. Available online: http:// www.ecochamps.eu/project (accessed on 26 10 2018).

11. Panda, K. C. Dealing with Noise and Vibration in Automotive Industry, 12th International Conference on Vibration Problems, ICOVP 2015, Proc. Engineering 2016, 144, pp. 1167 – 1174, doi: 10.1016/j.proeng.2016.05.092.

12. Genuit, K., Bray, W. R. A Virtual Car: Prediction of Sound and Vibration in an Interactive Simulation Environment, *J. of Passenger Car: Mechanical Systems J.* **2001**, 110, 6, pp. 1748-1754, www.jstor.org/stable/44731036

13. Schulte-Werning, B., Asmussen, B., Behr, W., Degen, K., Garburg R. Advancements in Noise and Vibration Abatement to Support the Noise Reduction Strategy of Deutsche Bahn, In book: Noise and Vibration Mitigation for Rail Transportation Systems (2012), DOI: 10.1007/978-4-431-53927-8_2.

14. Razak, N. F. D., Sani, M. S. M., Azmi, W. H., Zhang, B., Noise and vibration analysis for automotive radiator cooling fan, 4th International Conference on Mechanical Engineering Research (ICMER2017), IOP Conf. Series: Materials Science and Engineering 2017, *257*, 012083 doi:10.1088/1757-899X/257/1/012083.

15. Duffy, K. P., Padula, S. P., Scheiman, D. A., Damping of high-temperature shape memory alloys, *Proc. of SPIE - The International Society for Optical Engineering* **2008**, DOI: 10.1117/12.776288.

16. [Davino, D., Giustiniani, A., Visone, C., Adly, A. Experimental analysis of vibrations damping due to magnetostrictive based energy harvesting, *J. Applied Physics* **2011**, *109*, 07E509, doi: 10.1063/1.3545798.

17. Bein, T., Elliot, S., Ferralli, L., Casella, M., Meschke, J., Saemann, E. U., Nielsen, F. K., Kropp, W. Integrated solutions for Noise and Vibration control in vehicles, *Proc.-Social and Behaviour Sciences* **2012,** *48*, pp. 919-931, doi: 10.1016/j.sbspro.2012.06.1069.

18. Liao, Y., Sodano, H. A. Piezoelectric Damping of Resistively Shunted Beams and Optimal Parameters for Maximum Damping, *J. of Vibration and Acoustics* **2010**, *132*, 4, doi:10.1115/1.4001505.

19. Ciminello, M., Ameduri, S., Concilio, A. FE Modeling of an Innovative Vibration Control Shunt Technique, *J. of Intelligent Material Systems and Structures* **2007**, *19*, 8, pp. 875-887, https://doi.org/10.1177/1045389X07082379.

20. Ameduri, S., Diodati, G., Concilio, A. SMA Embedded Panel Optimized Through a Genetic Approach, *J. of Intelligent Material Systems and Structures* **2009**, *20*, 13, pp. 1529-1540, https://doi.org/10.1177/1045389X09337573

21. Jani, J., M., Leary, M., Subic, A. Shape Memory Alloys in Automotive Applications, *Applied Mechanics and Materials* **2014**, *663*,pp. 248-253, DOI: 10.4028/www.scientific.net/AMM.663.248.

22. Concilio, A., Ameduri, S., Influence of structural architecture on linear shape memory alloy actuator performance and morphing system layout optimization, *J. of Intelligent Material Systems and Structures* **2013**, *25*, 16,pp. 2037-2051, https://doi.org/10.1177/1045389X13517306

23. Timoshenko, S. P., Gere, J. M., *Theory of Elastic Stability*, 2nd ed., International Student Edition; Mc Graw-Hill International Book Company, 1985, pp 76-82, ISBN 0-07-Y85821-7.

24. Mirzaeifar, R., DesRoches, R., Yavari, A. A combined analytical, numerical, and experimental study of shape-memory-alloy helical springs, *Intern. J. of Solids and Structures* **2011,** *48*, pp. 611–624, https://doi.org/10.1016/j.ijsolstr.2010.10.026.

25. https://www.cira.it/en/research-infrastructures/vibro-acoustic-characterisation-laboratory.